Metals **2015**, *5*, 920-933; doi:10.3390/met5020920

OPEN ACCESS

metals

ISSN 2075-4701

www.mdpi.com/journal/metals/

Article

Mechanical and Structural Investigation of Porous Bulk Metallic Glasses

Baran Sarac [1,*], Daniel Sopu [1], Eunmi Park [1], Julia Kristin Hufenbach [1], Steffen Oswald [1], Mihai Stoica [1,2] and Jürgen Eckert [1,3]

[1] Institute for Complex Materials, Leibniz Institute for Solid State and Materials Research Helmholtzstrasse 20, D-01069 Dresden, Germany; E-Mails: d.sopu@ifw-dresden.de (D.S.); e.m.park@ifw-dresden.de (E.P.); j.k.hufenbach@ifw-dresden.de (J.K.H.); s.oswald@ifw-dresden.de (S.O.); m.stoica@ifw-dresden.de (M.S.); j.eckert@ifw-dresden.de (J.E.)

[2] Politehnica University of Timisoara, P-ta Victoriei 2, RO-300006 Timisoara, Romania

[3] TU Dresden, Institute of Materials Science, D-01062 Dresden, Germany

* Author to whom correspondence should be addressed; E-Mail: b.sarac@ifw-dresden.de; Tel.: +49-351-4659-1877; Fax: +49-351-4659-540.

Academic Editors: K. C. Chan and Jordi Sort Viñas

Received: 28 April 2015 / Accepted: 25 May 2015 / Published: 2 June 2015

Abstract: The intrinsic properties of advanced alloy systems can be altered by changing their microstructural features. Here, we present a highly efficient method to produce and characterize structures with systematically-designed pores embedded inside. The fabrication stage involves a combination of photolithography and deep reactive ion etching of a Si template replicated using the concept of thermoplastic forming. Pt- and Zr-based bulk metallic glasses (BMGs) were evaluated through uniaxial tensile test, followed by scanning electron microscope (SEM) fractographic and shear band analysis. Compositional investigation of the fracture surface performed via energy dispersive X-ray spectroscopy (EDX), as well as Auger spectroscopy (AES) shows a moderate amount of interdiffusion (5 at.% maximum) of the constituent elements between the deformed and undeformed regions. Furthermore, length-scale effects on the mechanical behavior of porous BMGs were explored through molecular dynamics (MD) simulations, where shear band formation is observed for a material width of 18 nm.

Keywords: bulk metallic glass; porous materials; Si lithography; thermoplastic forming; mechanical testing; shear band; microstructure; toughening mechanism; MD simulations; compositional analysis

1. Introduction

The effectiveness of a second phase in metallic glass structures, like foams and composites, to improve mechanical properties has been agreed upon widely. Unfortunately, the current methods used to fabricate such structures have insufficient control over the arrangement of microstructural features [1–4]. To overcome this challenge, a novel strategy to analyze microstructure-property relationships was postulated by Sarac *et al.* [5–8]. The strength and purpose of this method is the ability to vary microstructural features completely independently and to determine the individual effect of these features on the mechanical and morphological response, respectively. Bulk metallic glasses (BMGs) are excellent candidates for these investigations due to the intrinsic Newtonian flow behavior in their supercooled liquid region and the length-scale influence on properties [9]. In the micro-scale regime, the control mechanism of fracture in BMGs relies on the multiplication/deflection of the shear bands (SBs). These bands can be stabilized as long as the second phase spacing is less than the plastic zone size [10], creating a toughening mechanism in metallic glasses. Numerical simulations conducted by a non-local gradient-enhanced continuum mechanical model implemented by a finite element method [11,12] verify this proof of concept. The model sheds light on the scalability and versatility of this approach by using periodic boundary conditions along the external boundaries of the representative volume element [13] or by analyzing the spectrum of samples with stochastic pore designs [14]. In addition, the SB-mediated inhomogeneous plastic flow below the micron level is further regarded as the fundamental deformation mechanism for sub-micron-sized Zr-BMG pillars at no expense of yield strength [15].

The concept of thermoplastic forming has been broadly adopted for BMGs, which enabled a wide span of geometries on a ten orders of magnitude length scale [16]. This phenomenon has lately been utilized in a variety of micro- to nano-meter-scale applications, which can combine multiple length scale features in one component with easiness and precision via a thermoplastic forming (TPF) process [16,17]. The intrinsic properties in BMGs (*i.e.*, dramatic decrease in viscosity and increase in the formability at high temperatures) enhance the competitiveness of different TPF-based amorphous alloy processing within the commercial production routes [18].

The versatility in deformation behavior of BMGs is inherently related to the size effects, where the deformation is solely controlled by Newtonian flow behavior. Particularly interesting is the region where the deformation of the macro-sized samples, defined by global catastrophic fracture, turns into localized shear-induced deformation [6,7]. In this contribution, the toughening mechanism of the porous BMGs in terms of the mechanical and structural changes is investigated. The structural changes in the vicinity of shear bands and crack surfaces of the actual samples are sought to determine the influence of compositional alterations over the mechanical properties. Furthermore, molecular dynamics simulations will be carried out under uniaxial tension to understand the influence of porosity on the nanometer scale.

2. Materials and Methods

Intelligently-designed porous structures involve a unique fabrication strategy, which permits the arrangement of microstructural features within the BMG matrix with high precision and easiness. The layout drawings of these complex patterns was created by a CAD software (AutoCAD 2013, Autodesk Inc., San Rafael, CA, USA), which was subsequently transferred to a direct laser beam writer to fabricate the chromium glass photomask. Roughly, 50 samples with distinct pore designs were created on a 150-mm (or bigger) diameter template. Si wafers are utilized for this purpose, because of their low shrinkage, the precision in the directional etch, close tolerances to the original design and the cost-effectiveness of commercially-viable silicon. Figure 1a illustrates a small section of the Si wafer, where the entire wafer was coated uniformly by spinning PDMS photoresist. After the pre-baking process, the photoresist was patterned by UV exposure, where the selected regions of the photoresist were polymerized with the aid of the chromium mask. Figure 1b outlines the cured regions of the periodic circular pore design (in red), which become insoluble to the developer solution. The resist was then post-baked, and the uncured regions were stripped. Patterns with a depth of 400 μm were successively etched using deep reactive ion etching (Bosch process, Robert Bosch GmbH, Gerlingen, Germany), which allowed creating high-quality sidewall and top surface (roughness in hundreds of nanometers), as well as an anisotropic etch profile with a maximum span (pore diameter to etch length) ratio of 1:8. Figure 1c shows the sketch of the template with periodically-spaced pillars.

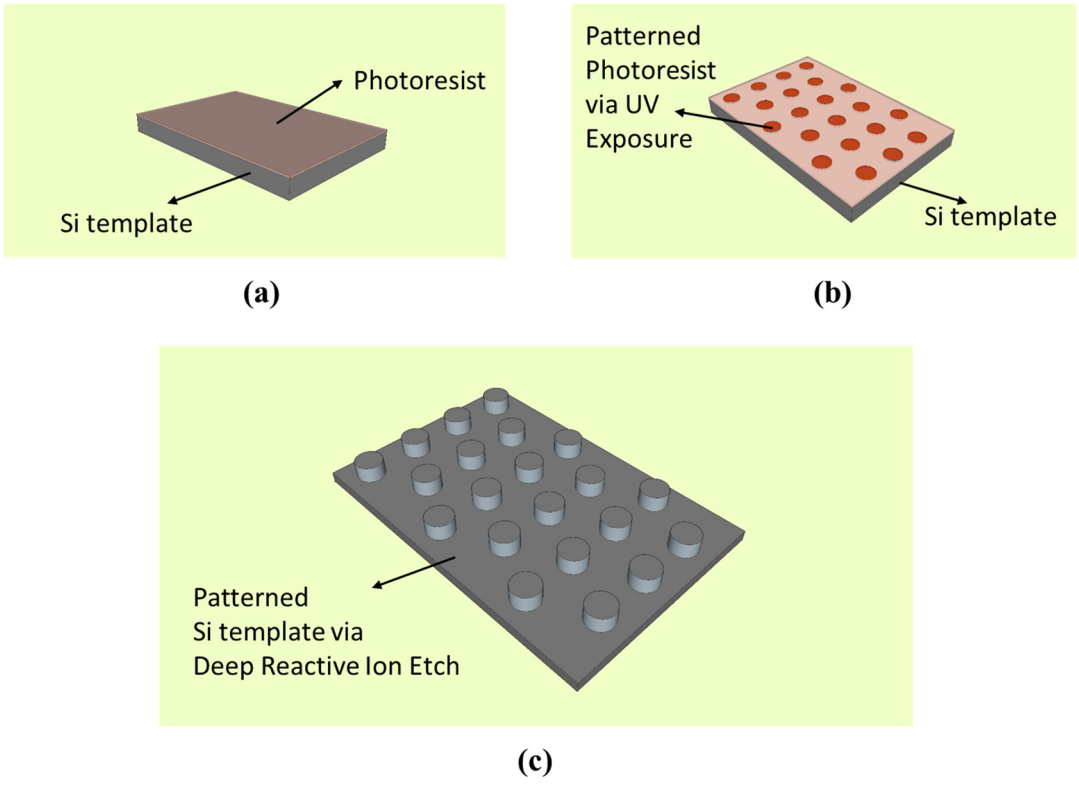

Figure 1. Patterning procedure of the periodic microfeatures. (**a**) Coating the Si template (wafer) surface with photoresist. (**b**) Patterning the photoresist using the chromium mask and UV light source. (**c**) Selective anisotropic etching of the entire Si template through deep reactive ion etching, which generates the negative pattern of the final structure.

For the manufacturing process, $Pt_{57.5}Cu_{14.7}Ni_{5.3}P_{22.5}$ was selected, because of its exclusively high fracture toughness $K_{1c} \approx 80$ MPam$^{1/2}$ and Poisson's ratio $v = 0.42$ in combination with low shear to bulk modulus ratio G/B = 0.168, placing this material into a different category, even among the BMG alloy families with proven records of extensive shear banding and plasticity [10,19]. In addition, a large processing window of ≈90 K and a large formability parameter S [20] enable this BMG alloy type to be used in pattern replication with high complexity and precision. The cast rods of this alloy were prepared in a quartz tube under a vacuum of 10^{-6} mbar, where the tube was purged with an inert gas to remove the residual oxygen. B_2O_3 is used to flux the ingot, which was confirmed to increase the glass forming ability by reducing the oxide content even to a higher extent [21]. The final diameter of the cast rod is 2 mm. The cast rod displays a broad peak in the X-ray diffraction (XRD) pattern, as well as a distinct glass transition and a sharp crystallization in the differential scanning calorimetry (DSC) curve. These findings are ascribed to the glassy nature of the as-cast state [22].

For comparison, $Zr_{35}Ti_{30}Cu_{7.5}Be_{27.5}$ metallic glass with relatively smaller fracture toughness K_{1c} of about 42.5 MPam$^{1/2}$ (averaged value from [5]), lower Poisson's ratio $v = 0.37$ and higher shear to bulk modulus ratio G/B = 0.285 was selected. This BMG type exhibits one of the widest supercooled regions of the known BMG types, rendering these materials to have excellent glass forming ability, as well as very low viscosity during hot forming (*viz*. 10^5 Pas) [23]. For this reason, it is suitable for rapid manufacturing of highly complex structures (including undercuts/multi-layered patterns) within very tight tolerances. The final rods of 10 mm in diameter, which were cast using copper mold suction casting in a Ti-gettered argon atmosphere, are fully amorphous [23]. The rods from both compositions were then sliced and hot-pressed to the desired thicknesses using an Instron compression device with a custom-built cartridge heating system. The pre-pressed BMG disc was situated on the patterned sample, and both were heated together to the TPF temperature of 550 K (Figure 2a). The viscous BMG flows into the etched regions as the applied stress (σ_{app}) exceeds the flow stress defined by the Newtonian flow rule:

$$\sigma_{app} > \sigma_{flow} = 3\eta\dot{\varepsilon} \quad (1)$$

where η is the viscosity of the BMG at TPF temperature and $\dot{\varepsilon}$ is the strain rate of the TPF. For strain rates of $10^{-1}s^{-1}$ or lower, σ_{flow} for BMGs with high formability (e.g., Zr- and Pt-based BMGs [20]) is calculated to be 0.3 MPa, placing them in the deformation scale of the commercially available polymers [13]. The sample with embedded pores was then detached from the assembly by BMG surface polishing (the polished Si-BMG assembly is given in Figure 2b) and subsequent Si etching using a diluted KOH (35% by mass) solution (Figure 2c). The middle section of the actual porous BMG sample (left) and the entire tensile sample (middle) is depicted in Figure 2d. Both samples remain fully amorphous after thermoplastic forming (Figure 2d, right). The samples were pinned from the grip sections, and the tensile test was conducted under quasi-static conditions of $\dot{\varepsilon} = 5 \times 10^{-3} s^{-1}$ until rupture.

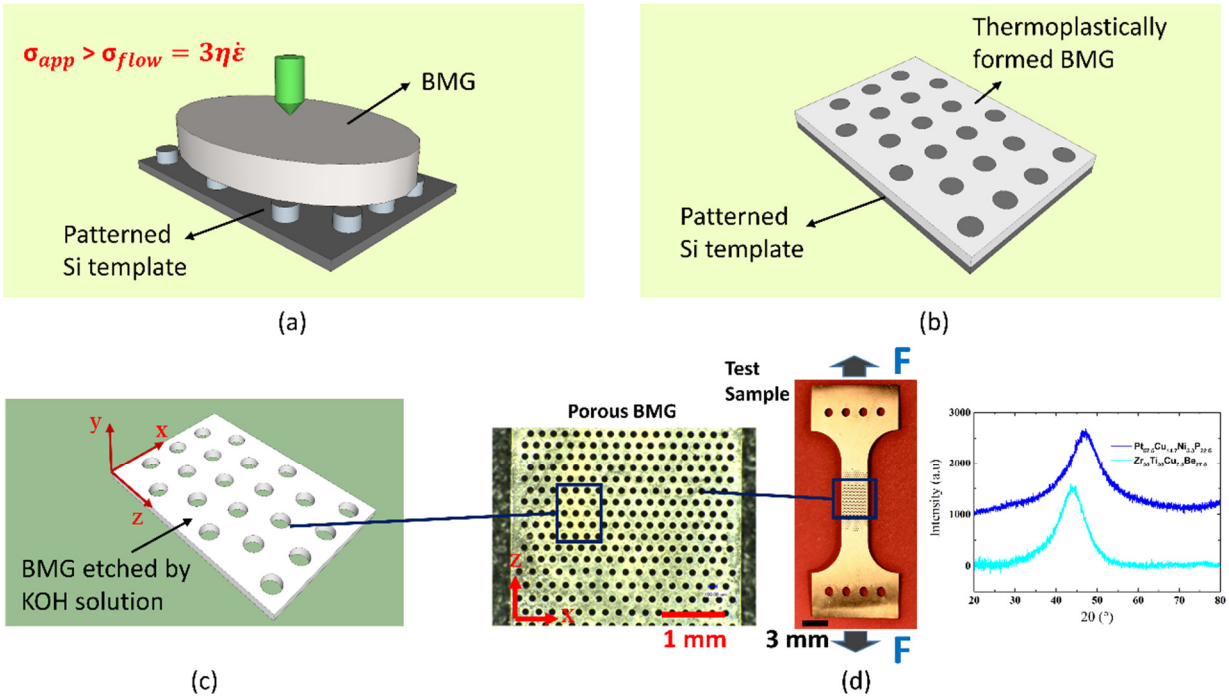

Figure 2. Thermoplastic forming of bulk metallic glasses (BMGs) into a complex geometry. (**a**) BMG disc placed on Si template with embedded negative pattern. (**b**) BMG is thermoplastically formed when the stress resisting the flow behavior σ_{flow} is exceeded. (**c**) Final sample shape is attained by metallographic treatment, and the sample is released from the Si template via KOH etching. (**d**) Actual sample geometry (middle) with the embedded periodic pores (left). The broad diffraction maximum after thermoplastic forming (right) reveals the fully amorphous nature of the alloys.

The chemical analysis of Pt-BMG is performed using a mixture of HCl (10 mL), HNO_3 (3 mL) and H_2O_2 (1 mL) added to deionized water. Four samples with approximately 50 mg are dissolved separately via microwave digestion at 513 K for 1 hour, where the total mass of these acidic solutions is 1000 g. The analysis of the dissolved elements is carried out through inductive coupled plasma optical emission spectroscopy (ICP-OES analysis), where the constituent elements are identified by their characteristic emission lines and quantified by the intensity of the same lines.

3. Results and Discussion

3.1. Influence of Pore Design

Earlier results revealed the importance of the pore design within the matrix [5,13]; the mechanical properties are optimized, as the diameter-to-spacing ratio (*d*/*s*) of the embedded pores is chosen to be between 0.5 and two. For this ideal range, the deformation is mainly controlled by the periodically-spaced pores, and thereby, the global fracture of the sample is delayed by the redirection of SBs and redistribution of the resolved shear stress around the pores. The decomposition of deformation into elastic and plastic parts through cyclic loading has demonstrated that the majority of the deformation is attributed to the geometric lineup of the pores (AB-type pore lineup, where the center of apore is

situated equidistant in x-direction to two pores in the neighboring row; see Figure 2d). The material remaining between the pores resembles a helical pattern, which creates additional elastic stretching compared to that of the sample with AA-type (center of the pores match between each row) pore stacking during tension [5]. The rest of the deformation is accumulated in the vicinity of the crack zone, where the SBs between the lateral pores perpendicular to the loading direction favor the additional macroscopic plasticity generation.

The quasi-static tensile behavior of BMG monolithic and porous structures for Pt- and Zr-BMGs is illustrated in a 3D stress-strain-absorbed energy per unit volume plot (Figure 3). The monolithic BMGs fabricated by thermoplastic forming exhibit an elastic limit of about 2% with no remarkable plastic deformation. On the other hand, the porous counterparts, including a periodic AB-type lineup with pore diameter and spacing of 100 and 50 μm (*i.e.*, d100s50), respectively, show almost 6% total strain at the expense of their fracture strength. The absorbed energy per unit volume is described by the area under the strain-stress curve until rupture, where the multiplication of these two components creates a second-degree parabolic profile. Further information pertaining to the mechanical and structural properties of these alloys can be found in Table 1.

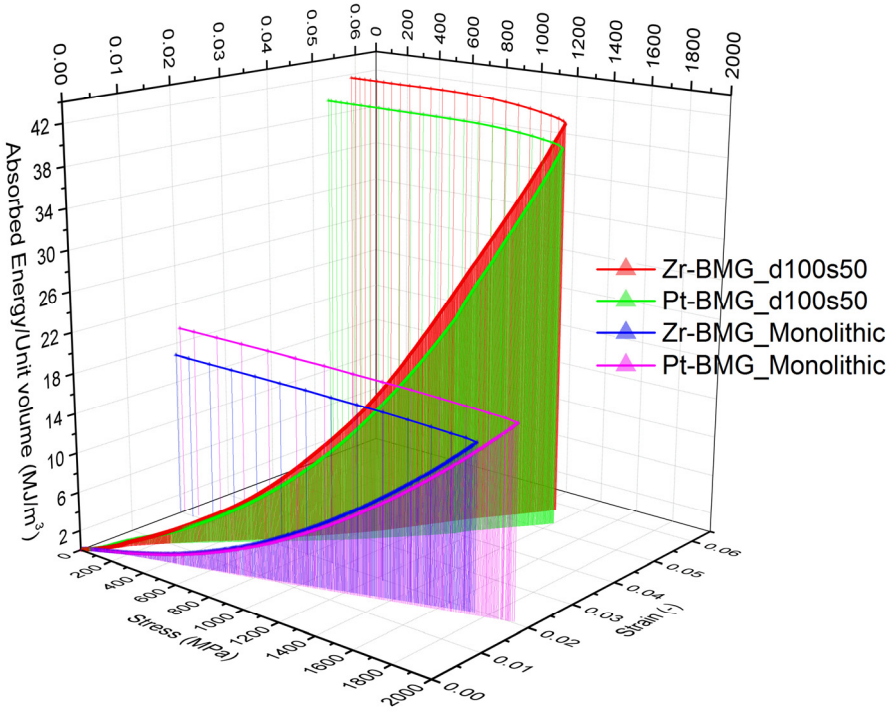

Figure 3. Representative graph of the deformation behavior of monolithic *vs*. porous Zr- and Pt-BMGs. Dimensions of the samples are within the same scale. $t \approx 300$ μm (sample thickness), $w = 3.75$ mm (width of porous BMG samples), $w = 3$ mm (width of Pt- and Zr-BMGs). The nominal fracture strength of the samples is calculated from the subtracted pore region where the shear bands (SBs) are connecting the pores perpendicular to the applied tensile load.

Table 1. Experimental parameters of the thermoplastically formed bulk (monolithic) and porous (d = 100 μm, s = 50 μm, d/s = 2) samples. The error percentages for σ_y and ε_y are within ±5%, whereas for W, the error is within ±10.5%.

Sample Name	σ_y (MPa)	ε_y (-)	E (GPa)	W (MJ/m^3)
Zr-BMG bulk	1741	0.019	87	16.8
Pt-BMG bulk	1924	0.020	95	19.4
Zr-BMG d100s50	1305	0.058	23	41.6
Pt-BMG d100s50	1399	0.053	28	39.6

The fracture analysis of Pt-BMG through scanning electron microscopy (LEO 1530 Gemini, Carl Zeiss, Oberkochen, Germany) reveals the characteristics of the multiple SB formation before fracture occurs. As an example, the network of pores via SB formation near the fracture surface is seen in Figure 4a. In this region, a number of around 20 SBs is observed (Figure 4b), where the local cleavage is ascribed to the high stress accumulation on the tip of an already existing SB (indicated with dark blue dotted region), which further develops and becomes irrepressible.

The phenomenon of hindering shear band propagation by an obstacle (e.g., *in situ* and *ex situ* second phases, heterogeneities, pores) is correlated with the intrinsic plastic zone size R_P defined by:

$$R_P = \frac{1}{\pi}\left(\frac{K_{1C}}{\sigma_y}\right)^2 \quad (2)$$

where K_{1c} is defined as the Mode 1 fracture toughness of the sample. Computing Equation (2) with the values for Pt-BMG and Zr-BMG results in R_P of 550 μm and 190 μm, respectively. Therefore, the second phase features become the prominent mechanism for the localized SB stabilization given that the spacing between the second phases are equal to or smaller than the intrinsic plastic zone size of each alloy type.

The fracture surface topology of the highly deformed Pt-BMG samples under uniaxial tension exhibit cores (indicated by white arrows) and radiating vein-like structures (Figure 4c). The cores represent the initial microcracks before fracture during tension [24]. The regions with a lava texture (pointed by black arrows in Figure 4d) appearing on the ridge of the veins confirm the molten phase of the Pt-BMG porous sample, which areattributed to localized melting generated by the elastic energy dissipated as heat on the fracture plane (as previously suggested in [25,26]), with an estimated temperature increase of 900 K [27]. Similar shear and fracture surface patterns are observed in Zr-BMG samples (Figure 5a–c). The smooth region accounts for the shear offset before global failure (which is also seen in Pt-BMGs; see the bottom part of Figure 4c) accompanied by vein-like deformation during fracture. The most significant difference between the fracture surfaces of two different alloys is that for the Zr-BMG, the molten spots are sparsely distributed within the vein-like patterns with a small and round shape, whereas for Pt-BMG, large molten regions scattered around veins are observed.

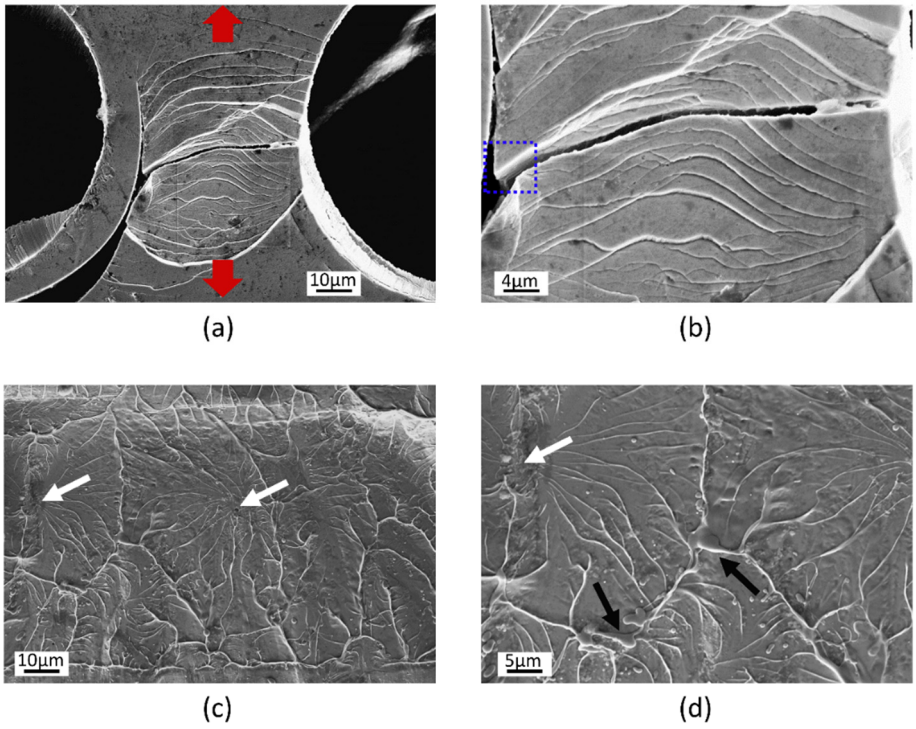

Figure 4. Morphological analysis of Pt-BMG pulled until rupture. (**a**,**b**) Deformation is localized to multiple SBs connecting adjacent pores perpendicular to the loading direction. (**c**,**d**) Fracture plane analysis shows the core regions (white arrows), as well as the vein-like deformation pattern containing molten regions (black arrows).

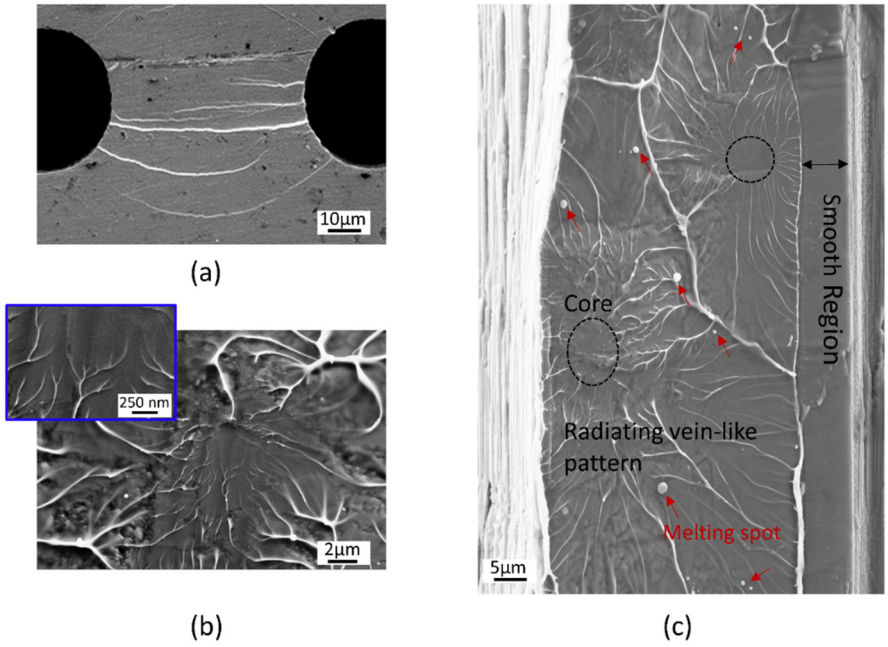

Figure 5. Morphological analysis of the Zr-BMG sample. (**a**) SBs are formed between pores perpendicular to loading, some of which further branch in multiple bands. (**b**) The ridges of the veins on the fracture surface radiate and point toward a core, where the tip of the veins has a width smaller than 50 nm (inset). (**c**) Fracture plane analysis shows various deformation morphologies, including melting spots.

3.2. Size Effects in Metallic Glasses

Next, it would be interesting to see how the tensile ductility of BMG changes when the characteristic length scale goes down to the nanometer regime. Since the critical crack length is in the order of micrometers, SB-mediated inhomogeneous flow is observed when approaching the nm scale [15]. We conducted molecular dynamics simulations in order to analyze the deformation behavior of bulk metallic glass heterostructures with pore sizes of 18 nanometers. The SB propagation and distribution across the pores were investigated for the ratio $d/s = 1$. As a prototype material, a CuZr BMG plate with dimensions of 36 nm × 7 nm × 85 nm, giving a total number of 1,172,450 atoms, was considered [28]. By using periodic boundary conditions, we excluded the presence of free surfaces that promote strain localization and formation of critical SBs [29]. Thus, the pores are the only heterogeneities in the BMG plate. The BMG heterostructure is deformed in tension along the z-direction with a strain rate of $\dot{\varepsilon} = 4 \times 10^7\ s^{-1}$. The stress-strain curve together with the local atomic shear strain calculated by OVITO (open visualization and analysis tool for atomistic simulations) [30] is presented in Figure 6.

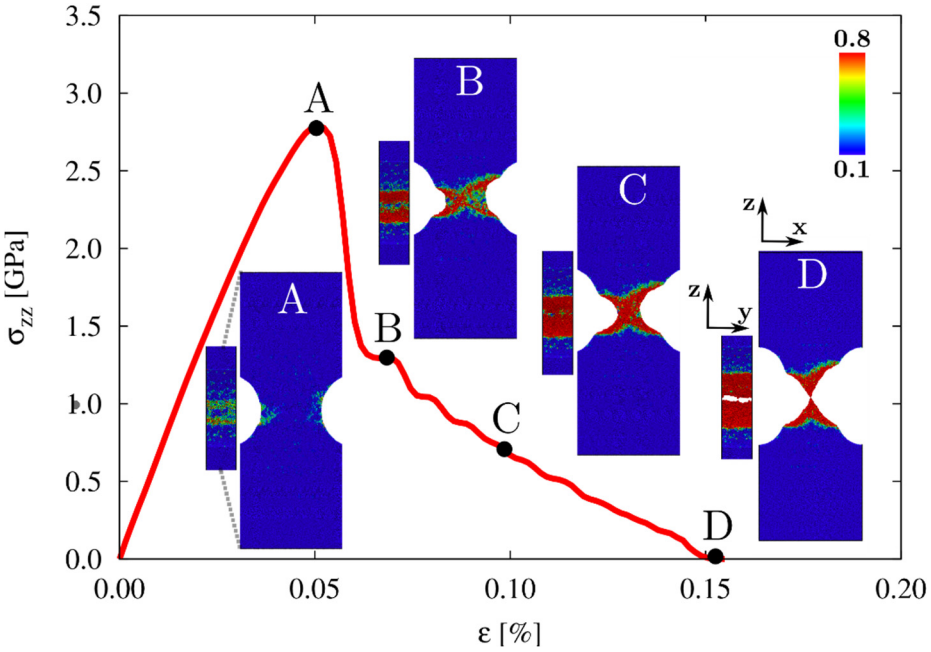

Figure 6. Deformation of a sample (in the z-direction) having pores of 18 nm in diameter. The front view (xz-plane) and side view (yz-plane) of each deformation pattern are displayed for different states of deformation. Note that the side view is scaled down, where the corresponding actual length is indicated by the dashed lines in the contour plots of Point A. Homogenous deformation (Point A), followed by two SBs intersecting each other (Point B) with a sudden decrease in strength. After this point, necking starts to prevail (Point C), and the failure occurs at a strain of 15% (Point D).

In order to investigate the deformation mechanism of nanoporous BMG, the most important four steps along the deformation are identified. Around 5% strain (Point A), when the maximum stress is achieved, two SBs start nucleating at the pore surface. This mechanism can be seen better by looking at the side of the plate (yz-plane). Increasing the strain to 7%, the two SB propagate along the x-direction

of the BMG plate. Basically, the SBs occur perpendicular to the loading direction as found in the case of the BMG with micron-sized pores, except that a large number of SBs were observed at the micron level. The intersection of two SBs causes the serrated-type deformation as observed between Points B and C. Since the pores have a diameter of just 18 nm and the critical SB width is about 4–5 nm [31], only two SBs are mediating the plasticity. Increasing the strain forward to 10%, the two SB overlap and give rise to necking of the BMG plate; see Point C. Finally, the BMG plate fails at a strain of 15% normal to the loading direction, as can be seen at Point D. In general, thermally-activated processes are excluded in MD simulations, resulting in a higher ultimate yield strength. The trends for the strain and elastic modulus are comparable to the experimental results of the porous structures. The presented shear-driven-type deformation at the nanoscale also explains why the vein-like shear below 50 nm can be observed on the fracture surface of the actual samples (Figure 5b, inset).

3.3. Compositional Investigation of Pt-BMG

To reveal the compositional fluctuations during thermomechanical (*viz*. thermoplastic forming) and room temperature tensile testing, energy dispersive X-ray analysis (EDX attached to SEM) was carried out on the fracture surface. We have chosen Pt-BMG based on the fractographic analysis, which shows higher amounts of molten regions, radiating vein-like patterns and SBs between the neighboring pores compared to those of the Zr-BMG. The concentration of each element was determined from the smooth deformation region indicating the SB evolvement (Figure 7a), as well as the vein-like patterns (Figure 7b) and molten regions (Figure 7c) generated by fracture. In comparison, EDX analysis of the undeformed region of the thermoplastically formed sample (Figure 7d) and chemical analysis of the as-cast sample (Table 2) were likewise performed. The EDX results reveal 5 at.% higher P content observed at the undeformed regions of the specimen and in as-cast state at the expense of Ni and Cu compared to the P content of the molten regions with ridges. The phosphorus deficiency is pronounced for the core regions, which are, as mentioned before, counted as the onset of microfractures. On the other hand, an enrichment in the Pt content (mean value by ≈2.5 at.%) is attained as the deformation proceeds from the shear-type deformation toward the core of the radiating vein-like deformation patterns. When the as-cast state sample (chemical analysis given in Table 2) is taken as a basis, the results also suggest that the influence of thermoplastic forming on the compositional fluctuation (the mean of the undeformed region in Table 2, Figure 7a) is much less significant compared to the compositional fluctuation of the uniaxially deformed tensile samples.

Auger spectral analysis (JEOL JAMP 9500F Scanning Auger Microprobe) also validates the increase in content of phosphorus compared to the deformed regions (Figure 7e and Table 2). A Schottky field emission electron gun at 10 keV and 10 nA excited the metallic glass under 10^{-7} Pa vacuum, where a differentially-pumped ion gun with 1 keV was used to sputter argon ions onto the Pt-BMG at a sputtering rate of 8 nm/min for surface cleaning. Elastically-scattered electrons penetrated the material to a depth of 1 μm. Different from EDX, the Auger information comes only from the first nanometer thickness, where measurements are conducted after removing the surface contamination. Because of the use of a standard single element sensitivity factor, not validated for this special alloy, and possible concentration changes by preferential sputtering, the determined concentration are different from the EDX data. Moreover, the Ni peaks are overlaid by Cu and can only be detected by low efficiency peaks. For this

reason, the comparison is made by the normalized n_P/n_{Pt} ratio. A decreasein this ratio (as in the case of EDX measurements) also confirms this P decifiency and Pt enrichment, particularly on the vein-like, core and molten regions.

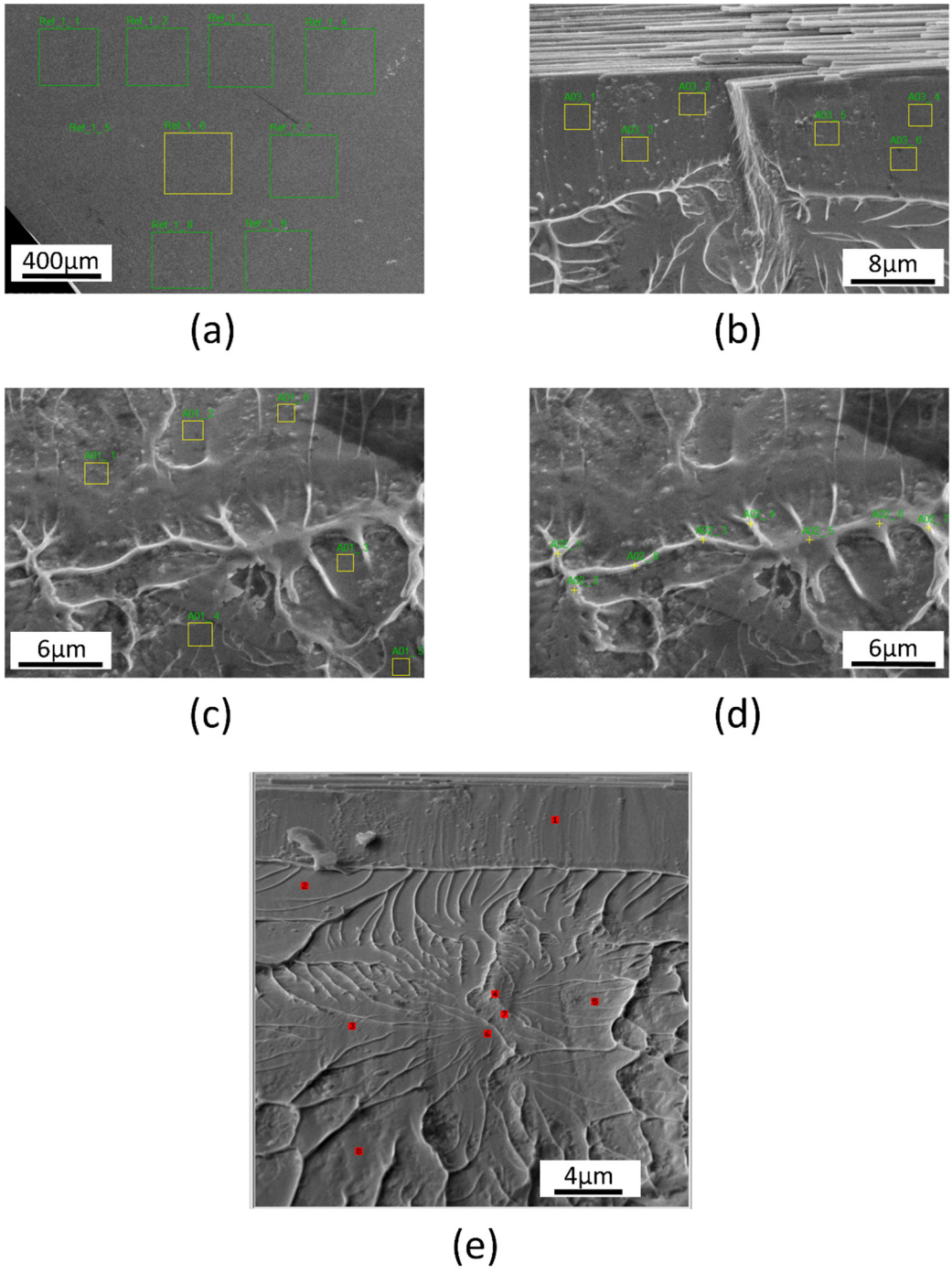

Figure 7. EDX analyses of the fracture surface of the porous Pt-BMG taken from the (**a**) undeformed surface, (**b**) smooth region, (**c**) vein-like region and (**d**) ridges of veins and molten regions. (**e**) Different fracture regions of interest obtained from Auger electron spectroscopy analysis. Point and region measurements were conducted depending on the specific area, where the numbers indicated are simply showing different measurements of interest within the same region.

Table 2. Concentration data of constituent elements of the Pt-BMG averaged from the deformed and undeformed regions. Chemical analysis reflects the as-cast state composition.

Element	Pt	Cu	Ni	P	n_P/n_{Pt}
Chemical analysis (at.%)	57.0 ± 0.4	14.4 ± 0.1	5.2 ± 0.1	23.4 ± 0.1	0.41
EDX Spectra (at.%) (Figure 7a–d)					
mean of undeformed region (Figure 7a)	56.0	14.6	5.5	23.9	0.43
mean of smooth region (Figure 7b)	55.5	15.4	6.8	22.3	0.40
mean of vein-like region (Figure 7c)	57.3	16.2	6.3	20.2	0.35
mean of ridges + molten regions(Figure 7d)	58.4	16.4	6.4	18.8	0.32
Auger spectra (at.%) (Figure 7e)					
mean of undeformed region	73.3	6.4	5.4	14.9	0.20
mean of smooth region	75.6	6.0	5.6	12.8	0.17
mean of vein-like region	76.9	6.1	5.3	11.7	0.15
mean of core + molten regions	76.4	6.4	5.2	12.0	0.16

4. Conclusions

This contribution highlighted the influence of pore design on the overall mechanical, fractographic and chemical properties. Replication of complicated patterns using a Si template provides a versatile toolbox to manipulate the properties of the metallic glasses in a controlled manner. The complex deformation state and the geometrical effect attributed to the pore lineup leads to multiple SB formations between neighboring pores perpendicular to loading, which increases the fracture strain by almost three times. Fracture surface analysis has identified three different deformation patterns, namely smooth region, vein-like pattern and core of the shear. Molten spots or regions were observed depending on the type of BMG analyzed. It has been confirmed by EDX and Auger spectra that the mechanically-induced plasticity causes variations among the constituent elements between deformed and undeformed regions up to 5 at%. Finally, MD simulations conducted with a similar d/s ratio sample depict SB formation followed by necking of the sample, where the SEM fracture surface observations have proven the shear-induced type of deformation below the 50 nm level.

Acknowledgments

The support for this work provided by the European Research Council under the Advanced Grant "INTELHYB–Next Generation of Complex Metallic Materials in Intelligent Hybrid Structures" (Grant ERC-2013-ADG-340025) is gratefully acknowledged. The authors thank Romy Keller for SEM imaging of BMGs, Andrea Voss for the chemical analysis of the as-cast Pt-BMG rod, Long Zhang for the XRD measurement of Pt-BMG sample and Junhee Han for the discussion and assistance regarding the EDX analysis.

Author Contributions

Baran Sarac wrote and edited the paper and contributed to all activities. Daniel Sopu performed the MD simulations. Eunmi Park and Julia Kristin Hufenbach contributed to the SEM and EDX analysis. Eunmi Park contributed to the XRD analysis. Steffen Oswald performed the Auger Spectroscopy

analysis. Steffen Oswald, Daniel Sopu and Julia Kristin Hufenbach contributed to the discussions. Jürgen Eckert and Mihai Stoica contributed to the interpretation and discussion of the results.

Conflicts of Interest

The authors declare no conflict of interest.

References

1. Schwarz, M.; Karma, A.; Eckler, K.; Herlach, D.M. Physical-mechanism of grain-refinement in solidification of undercooled melts. *Phys. Rev. Lett.* **1994**, *73*, 1380–1383.
2. Schroers, J.; HollandMoritz, D.; Herlach, D.M.; Grushko, B.; Urban, K. Undercooling and solidification behaviour of a metastable decagonal quasicrystalline phase and crystalline phases in Al-Co. *Mat. Sci. Eng. A* **1997**, *226*, 990–994.
3. Hofmann, D.C.; Suh, J.Y.; Wiest, A.; Duan, G.; Lind, M.L.; Demetriou, M.D.; Johnson, W.L. Designing metallic glass matrix composites with high toughness and tensile ductility. *Nature* **2008**, *451*, 1085–1089.
4. Hays, C.C.; Kim, C.P.; Johnson, W.L. Microstructure controlled shear band pattern formation and enhanced plasticity of bulk metallic glasses containing *in situ* formed ductile phase dendrite dispersions. *Phys. Rev. Lett.* **2000**, *84*, 2901–2904.
5. Sarac, B.; Schroers, J. Designing tensile ductility in metallic glasses. *Nat. Commun.* **2013**, *4*, 1–7.
6. Sarac, B.; Ketkaew, J.; Popnoe, D.O.; Schroers, J. Honeycomb structures of bulk metallic glasses. *Adv. Funct. Mater.* **2012**, *22*, 3161–3169.
7. Sarac, B.; Schroers, J. From brittle to ductile: Density optimization for Zr-BMG cellular structures. *Scr. Mater.* **2013**, *68*, 921–924.
8. Sarac, B. *Microstructure-Property Optimization in Metallic Glasses*; Springer Theses; Springer International Publishing: Cham, Switzerland, 2015; Volume XIII, p 87.
9. Schroers, J. Bulk metallic glasses. *Phys. Today* **2013**, *66*, 32–37.
10. Lewandowski, J.J.; Wang, W.H.; Greer, A.L. Intrinsic plasticity or brittleness of metallic glasses. *Philos. Mag. Lett.* **2005**, *85*, 77–87.
11. Svendsen, B.; Bargmann, S. On the continuum thermodynamic rate variational formulation of models for extended crystal plasticity at large deformation. *J. Mech. Phys. Solids* **2010**, *58*, 1253–1271.
12. Bargmann, S.; Ekh, M.; Runesson, K.; Svendsen, B. Modeling of polycrystals with gradient crystal plasticity: A comparison of strategies. *Philos. Mag.* **2010**, *90*, 1263–1288.
13. Sarac, B.; Klusemann, B.; Xiao, T.; Bargmann, S. Materials by design: An experimental and computational investigation on the microanatomy arrangement of porous metallic glasses. *Acta Mater.* **2014**, *77*, 411–422.
14. Sarac, B.; Wilmers, J.; Bargmann, S. Property optimization of porous metallic glasses via structural design. *Mater. Lett.* **2014**, *134*, 306–310.
15. Dubach, A.; Raghavan, R.; Loffler, J.F.; Michler, J.; Ramamurty, U. Micropillar compression studies on a bulk metallic glass in different structural states. *Scr. Mater.* **2009**, *60*, 567–570.

16. Kumar, G.; Desai, A.; Schroers, J. Bulk metallic glass: The smaller the better. *Adv. Mater.* **2011**, *23*, 461–476.
17. Hasan, M.; Schroers, J.; Kumar, G. Functionalization of metallic glasses through hierarchical patterning. *Nano Lett.* **2015**, *15*, 963–968.
18. Schroers, J. Processing of bulk metallic glass. *Adv. Mater.* **2010**, *22*, 1566–1597.
19. Schroers, J. Ductile Bulk Metallic Glass. *Phys. Rev. Lett* **2004**, *93*, 255506.
20. Schroers, J. On the formability of bulk metallic glass in its supercooled liquid state. *Acta Mater.* **2008**, *56*, 471–478.
21. Legg, B.A.; Schroers, J.; Busch, R. Thermodynamics, kinetics, and crystallization of $Pt_{57.3}Cu_{14.6}Ni_{5.3}P_{22.8}$ bulk metallic glass. *Acta Mater.* **2007**, *55*, 1109–1116.
22. Sarac, B.; Kumar, G.; Hodges, T.; Ding, S.Y.; Desai, A.; Schroers, J. Three-dimensional shell fabrication using blow molding of bulk metallic glass. *J. Microelectromech. S* **2011**, *20*, 28–36.
23. Duan, G.; Wiest, A.; Lind, M.L.; Li, J.; Rhim, W.K.; Johnson, W.L. Bulk metallic glass with benchmark thermoplastic processability. *Adv. Mater.* **2007**, *19*, 4272–4275.
24. Qu, R.T.; Stoica, M.; Eckert, J.; Zhang, Z.F. Tensile fracture morphologies of bulk metallic glass. *J. Appl. Phys.* **2010**, *108*, 063509.
25. Zhang, Z.F.; Eckert, J.; Schultz, L. Difference in compressive and tensile fracture mechanisms of $Zr_{59}Cu_{20}Al_{10}Ni_8Ti_3$ bulk metallic glass. *Acta Mater.* **2003**, *51*, 1167–1179.
26. Wright, W.J.; Saha, R.; Nix, W.D. Deformation mechanisms of the $Zr_{40}Ti_{14}Ni_{10}Cu_{12}Be_{24}$ bulk metallic glass. *Mater. Trans.* **2001**, *42*, 642–649.
27. Liu, C.T.; Heatherly, L.; Easton, D.S.; Carmichael, C.A.; Schneibel, J.H.; Chen, C.H.; Wright, J.L.; Yoo, M.H.; Horton, J.A.; Inoue, A. Test environments and mechanical properties of Zr-base bulk amorphous alloys. *Metall. Mater. Trans. A* **1998**, *29*, 1811–1820.
28. Mendelev, M.I.; Rehbein, D.K.; Ott, R.T.; Kramer, M.J.; Sordelet, D.J. Computer simulation and experimental study of elastic properties of amorphous Cu-Zr alloys. *J. Appl Phys.* **2007**, *102*, 093518.
29. Sopu, D.; Karsten, A. Influence of grain size and composition, topology and excess free volume on the deformation behavior of Cu–Zr nanoglasses. *Beilstein J. Nanotechnol.* **2015**, *6*, 537–545.
30. Stukowski, A. Visualization and analysis of atomistic simulation data with OVITO—The open visualization tool. *Model. Simul. Mater. Sci.* **2010**, *18*, 015012.
31. Shi, Y.F. Size-independent shear band formation in amorphous nanowires made from simulated casting. *Appl. Phys. Lett.* **2010**, *96*, 121909.